

Experimental study of $^{38}\text{Ar} + \alpha$ reaction cross sections relevant to the ^{41}Ca abundance in the solar system

R. Talwar,^{1,*} M. J. Bojazi,² P. Mohr,^{3,4} K. Auranen,¹ M. L. Avila,¹ A. D. Ayangeakaa,^{1,†} J. Harker,⁵ C. R. Hoffman,¹ C. L. Jiang,¹ S. A. Kuvin,⁶ B. S. Meyer,² K. E. Rehm,¹ D. Santiago-Gonzalez,^{7,1} J. Sethi,⁵ C. Ugalde,⁸ and J. R. Winkelbauer⁹

¹Physics Division, Argonne National Laboratory, Argonne, Illinois 60439, USA

²Department of Physics and Astronomy, Clemson University, Clemson, South Carolina 29634, USA

³Diakonie-Klinikum, Schwäbisch Hall D-74523, Germany

⁴Institute for Nuclear Research ATOMKI, Debrecen H-4001, Hungary

⁵Department of Chemistry and Biochemistry, University of Maryland, College Park, Maryland 20742, USA

⁶Department of Physics, University of Connecticut, Storrs, Connecticut 06269, USA

⁷Department of Physics and Astronomy, Louisiana State University, Baton Rouge, Louisiana 70803, USA

⁸Department of Physics, University of Illinois at Chicago, Chicago, Illinois 60607, USA

⁹Neutron Science Center, Los Alamos National Laboratory, Los Alamos, New Mexico 87545, USA



(Received 20 September 2017; revised manuscript received 26 March 2018; published 8 May 2018)

In massive stars, the $^{41}\text{Ca}(n,\alpha)^{38}\text{Ar}$ and $^{41}\text{K}(p,\alpha)^{38}\text{Ar}$ reactions have been identified as the key reactions governing the abundance of ^{41}Ca , which is considered as a potential chronometer for solar system formation. So far, due to experimental limitations, the $^{41}\text{Ca}(n,\alpha)^{38}\text{Ar}$ reaction rate is solely based on statistical model calculations. In the present study, we have measured the time-inverse $^{38}\text{Ar}(\alpha,n)^{41}\text{Ca}$ and $^{38}\text{Ar}(\alpha,p)^{41}\text{K}$ reactions using an active target detector. The reactions were studied in inverse kinematics using a 133-MeV ^{38}Ar beam and ^4He as the active-gas target. Both excitation functions were measured simultaneously in the energy range of $6.8 \leq E_{\text{c.m.}} \leq 9.3$ MeV. Using detailed balance the $^{41}\text{Ca}(n,\alpha)^{38}\text{Ar}$ and $^{41}\text{K}(p,\alpha)^{38}\text{Ar}$ reaction rates were determined, which suggested a 20% increase in the ^{41}Ca yield from massive stars.

DOI: [10.1103/PhysRevC.97.055801](https://doi.org/10.1103/PhysRevC.97.055801)

I. INTRODUCTION

A number of short-lived radionuclides (^7Be , ^{41}Ca , ^{26}Al , ^{36}Cl , etc.) existed at the time of the early solar system [1]. The origin and relative abundances of these radionuclides form the basis of solar system chronology and provide key information with respect to the birth environment of the sun [2]. These extinct radioisotopes could have become a part of the solar system in various ways, such as nucleosynthetic products from a supernova, asymptotic giant branch (AGB) star, Wolf-Rayet star, or background molecular clouds, and/or as a result of nuclear reactions between energetic charged particles and ambient gas or dust near the protosun [3–5].

^{41}Ca is one of the shortest-lived radionuclides ($t_{1/2} = 0.1$ Myr) for which firm evidence exists in early solar system materials. Hence, it provides key constraints on the timescale of last nucleosynthetic addition to the solar nebula [1]. Since ^{41}Ca can be found to have existed only in the oldest materials and then in very small concentrations, experimentally detecting ^{41}Ca is challenging. The origin of ^{41}Ca still remains a matter of debate with theory suggesting its production via either stellar nucleosynthesis or *in situ* irradiation. Such contrasting origins

have different implications for the solar system formation. In the case of stellar origin, a uniform ^{41}Ca abundance in the solar nebula would be useful for chronology as well as provide stringent constraints on the time span between its nucleosynthesis and inclusion into early solar system materials. An origin by *in situ* irradiation would lead to a ^{41}Ca heterogeneity in the nebula, thereby making chronological interpretations complicated [2]. In order to develop a better understanding of its origin and distribution as well as its relation to other short-lived radionuclides, further studies are needed with respect to the production mechanism of ^{41}Ca and its abundance in the oldest solar system materials, namely Ca-Al-rich inclusions (CAIs) found in primitive meteorites.

The first unambiguous evidence of ^{41}Ca was demonstrated by the correlated excesses of the daughter nucleus, ^{41}K , with Ca/K abundance ratios in Efremovka Type B CAIs [6]. Subsequent studies established the presence of ^{41}Ca in CM2 (Murchinson) hibonite grains. During these early works, small-geometry secondary-ion mass spectrometers (SIMSs) were used to study the ^{41}Ca abundances in CAIs. The results indicated an initial abundance ratio of $^{41}\text{Ca}/^{40}\text{Ca} = (1.41 \pm 0.14) \times 10^{-8}$ in the solar nebula. It was also observed that the presence of short-lived ^{26}Al and ^{41}Ca in some mineral phases, and absence in others, were correlated [7,8]. Since an initial abundance ratio of $^{26}\text{Al}/^{27}\text{Al} \sim 5.2 \times 10^{-5}$ in the solar nebula could be due to external seeding of ^{26}Al followed by hydrodynamic mixing [9,10], it was concluded that ^{41}Ca could

*85.rashi@gmail.com

†Present Address: Department of Physics, United States Naval Academy, Annapolis, Maryland 21402, USA.

also be derived from an external source [7]. These findings were further supported by a recent reanalysis of the CAI samples with a large-geometry SIMS [11]. After correcting for the resetting time calculated from the subcanonical $^{26}\text{Al}/^{27}\text{Al}$ ratio reported in Refs. [12,13], it was found that the $^{41}\text{Ca}/^{40}\text{Ca}$ ratio converges towards a value of $\sim 4.2 \times 10^{-9}$ [11]. This value is consistent with the $^{41}\text{Ca}/^{40}\text{Ca}$ ratio in the Allende CAI [14], characterized by a ratio of $(5.29 \pm 0.39) \times 10^{-5}$ for $^{26}\text{Al}/^{27}\text{Al}$ [15]. Consequently, Liu *et al.* [11] emphasized that ^{26}Al and ^{41}Ca must have been simultaneously incorporated into the solar system as stellar products.

More recently, though, and in contradiction to the previous findings [7,8], an analysis of Type A CAIs has revealed that ^{41}Ca abundances are not correlated with the $^{26}\text{Al}/^{27}\text{Al}$ ratios [2]. Based on this finding [2] it appears the distribution of ^{41}Ca is nonuniform throughout the solar nebula. Such heterogeneity can be explained if, unlike ^{26}Al , ^{41}Ca is an irradiation product [2]. Strong evidence of intense irradiation in the early solar system is derived from the high, but variable abundances of ^{10}Be ($t_{1/2} = 1.39$ Myr) inferred from CAIs [13,16,17]. Irradiation by gradual and impulsive flares from the sun on targets with CAI-like composition can also be conducive to production of ^{41}Ca in addition to ^{10}Be , but not ^{26}Al [2]. However, this model fails to explain the ^{41}Ca abundances inferred from Type B CAIs by Liu *et al.* [11]. An assortment of plausible scenarios have been presented to explain the observed heterogeneity in Type A CAIs [2], yet all corresponding conclusions are based on ^{26}Al and ^{41}Ca data available from a limited number of CAIs. Hence, it has proven challenging to determine the origin and production mechanism of these short-lived radionuclides, specifically ^{41}Ca , as its short half-life makes it exceedingly difficult to detect experimentally.

From the measurement of potassium isotopes in Ca-rich oxide grains (hibonites), Wasserburg *et al.* [4] had suggested AGB stars as one of the promising astrophysical environments for ^{41}Ca production. The probability of an AGB star contributing ^{26}Al (and ^{41}Ca) to the early solar cloud, however, is much less than one percent unless AGB star winds trigger star formation [18]. A more plausible scenario is that one or more massive stars contributed ^{41}Ca to the forming solar system since such massive stars are routinely associated with star-forming regions. Calcium-41 could be produced in *s*-process nucleosynthesis in the pre-supernova evolution of the star and ejected either in Wolf-Rayet phase winds before the supernova explosion or relatively unaltered in the outflow from the explosion. The bulk of the ^{41}Ca ejected from a massive star, however, is produced via shock-induced explosive oxygen-burning nucleosynthesis during the supernova event.

Apart from CAIs, primitive meteorites also contain micron-sized presolar grains, whose isotopic anomalies show that they condensed in the outflows from stellar environments [19]. Among the various types of presolar grains are low-density graphite grains with excesses in ^{44}Ca , which clearly demonstrates that these tiny particles condensed with ^{44}Ti in outflows from the supernova explosions of massive stars [20,21]. The authors of Ref. [22] found five low-density graphite grains that had excesses of ^{41}K , which they attributed to condensation of the grains with ^{41}Ca . This result provides further proof of a supernova origin for these grains, and the abundance of ^{41}Ca in

the grains yields important constraints on the mixing between supernova zones before grain condensation.

These considerations strongly suggest that massive stars play a key role in the production of ^{41}Ca in the galaxy. It is then natural to ask what reaction rates govern the yield of ^{41}Ca in massive stars. By following the techniques from Ref. [23], we performed a sensitivity study to understand the key reactions involved in ^{41}Ca production in a $25\text{-}M_{\odot}$ star during explosive nucleosynthesis following shock passage. Our study revealed that $^{41}\text{Ca}(n,\alpha)^{38}\text{Ar}$ and $^{41}\text{K}(p,\alpha)^{38}\text{Ar}$ reactions have a significant impact on the ^{41}Ca yield in explosive scenarios. Until now, due to experimental limitations, the thermonuclear rate for the $^{41}\text{Ca}(n,\alpha)^{38}\text{Ar}$ reaction has been derived using statistical-model calculations based on optical-model parameters chosen to fit experimental data for the $^{41}\text{K}(p,\alpha)^{38}\text{Ar}$ reaction [24]. In the present paper, we report on an experimental study of the time inverse $^{38}\text{Ar}(\alpha,n)^{41}\text{Ca}$ and $^{38}\text{Ar}(\alpha,p)^{41}\text{K}$ reaction cross sections in inverse kinematics. Based on these cross sections and detailed balance we provide the astrophysical reaction rates for $^{41}\text{Ca}(n,\alpha)^{38}\text{Ar}$ and $^{41}\text{K}(p,\alpha)^{38}\text{Ar}$ reactions and discuss their influence on the ^{41}Ca yield from massive stars.

II. EXPERIMENTAL SETUP AND RESULTS

The measurement was carried out at the ATLAS facility at Argonne National Laboratory. A 133-MeV ^{38}Ar beam was delivered to a MUlti-Sampling Ionization-Chamber (MUSIC) detector filled with 370 Torr of ^4He gas. MUSIC is an active-target detector consisting of a cathode, a Frisch grid, and an anode. It has close to 100% detection efficiency and has previously been used in studying (α,p) and (α,n) reactions of astrophysical interest [25].

As the beam particles travel through the chamber volume, the electrons resulting from the ionization of the ^4He gas molecules drift through the Frisch grid towards the anode, which is subdivided into 18 strips (strip 0–strip 17). Each strip provides measurement at a specific beam energy, as the beam loses energy through the detector. In this manner the anode allows us to measure a large energy range of the excitation function with a single incident beam energy [26]. Furthermore strips 1–16 are segmented into asymmetric left and right sections, as shown in Fig. 1. Such asymmetric segmentation helps produce a well-developed pattern of energy-loss signals corresponding to the beam as well as distinguish between different multiplicity events in the detector [27]. Further details

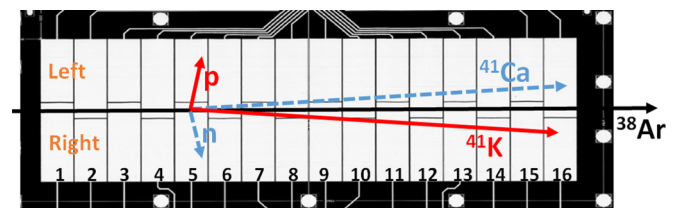


FIG. 1. Schematic of the asymmetric segmentation of the anode strips 1–16 inside the MUSIC detector. The black line shows the ^{38}Ar beam going through the center of the detector and the red and blue lines (solid and dashed, respectively) show the outgoing reaction particles for a reaction occurring in strip 5.

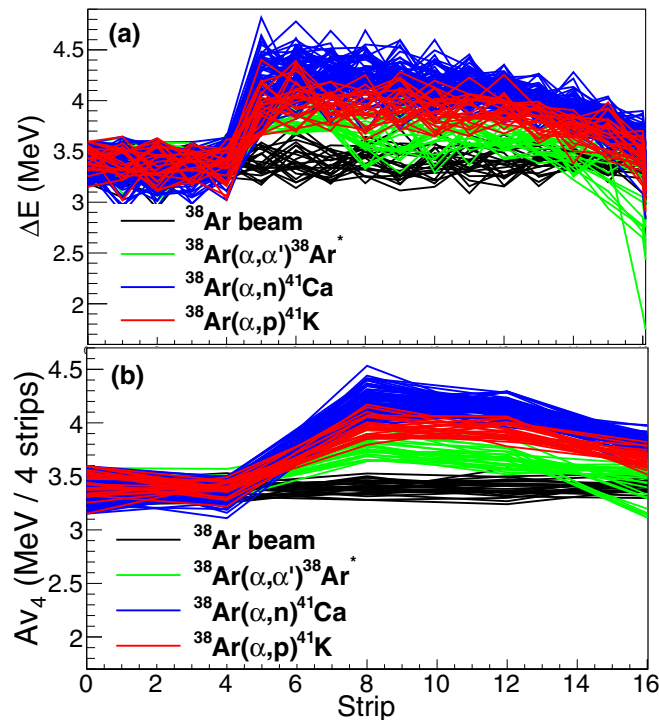


FIG. 2. The top panel (a) shows the ΔE signals measured over 16 strips of the MUSIC detector from $^{38}\text{Ar}(\alpha, n)^{41}\text{Ca}$ (blue), $^{38}\text{Ar}(\alpha, p)^{41}\text{K}$ (red), and $^{38}\text{Ar}(\alpha, \alpha')^{38}\text{Ar}^*$ (green) reactions occurring in strip 5, along with the beam (black). The ΔE values of all strips have been normalized to the ΔE value in strip 0. The bottom panel (b) is the same as (a), but averaged over four consecutive strips (Av_4).

of the detector's design and its operating principle can be found in Ref. [28].

The experiment was performed in inverse kinematics, i.e., bombarding the ^4He gas with the ^{38}Ar beam. Typical beam intensities of 3000–5000 particles/s were used in order to avoid pileup. The beam intensity was reduced using a series of pepper-pot attenuators along with the ATLAS beam sweeper, which increased the pulse period of the beam from 82 ns to 41 μs . Under these conditions, both the (α, n) (Q value = -5.223 MeV) and (α, p) (Q value = -4.019 MeV) channels were open, thus allowing us to study both reactions simultaneously covering an energy range in the center of mass of $E_{c.m.} = 6.8$ – 9.3 MeV.

As the ^{38}Ar beam interacts with the ^4He gas inside MUSIC, event traces corresponding to $^{38}\text{Ar}(\alpha, n)^{41}\text{Ca}$ (blue), $^{38}\text{Ar}(\alpha, p)^{41}\text{K}$ (red), and $^{38}\text{Ar}(\alpha, \alpha')^{38}\text{Ar}^*$ (green) reactions are separated on the basis of the differences in the energy-loss signals (ΔE) in each strip of the detector. In addition to these event traces, we also detect traces corresponding to the ^{38}Ar beam (black). This is illustrated in the Fig. 2 showing traces from the various reactions occurring in strip 5 of the MUSIC detector over a measuring period of 7 h, along with the beam traces. For a better visualization only the first 25 (α, α') and 25 beam traces are shown. Also, the ΔE values of all the strips in this figure have been normalized to the ΔE value in strip 0. Since the beam particles were counted simultaneously,

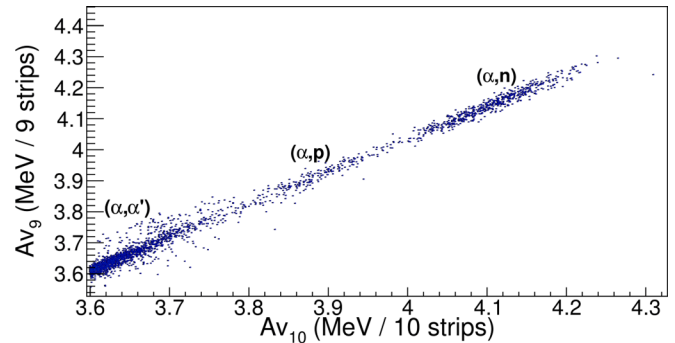


FIG. 3. Two-dimensional plot of ΔE values for events occurring in strip 5 averaged over ten (Av_{10}) and nine strips (Av_9), respectively, to improve the separation between events corresponding to the $^{38}\text{Ar}(\alpha, \alpha')^{38}\text{Ar}^*$, $^{38}\text{Ar}(\alpha, p)^{41}\text{K}$, and $^{38}\text{Ar}(\alpha, n)^{41}\text{Ca}$ reactions.

there were no additional monitor detectors needed for the normalization of the cross sections.

As can be seen in the top panel of Fig. 2, the event traces from different reactions are affected by fluctuations, which reflect uncertainties associated with the gain matching, the calibration of the 18 anode strips, and the emission angle of the reaction products. Such fluctuations can lead to a misinterpretation of various traces. In order to improve the separation among the three reaction channels, we averaged the ΔE values over a certain number of strips following the strip where the reaction took place. As an illustration, in the bottom panel of Fig. 2, we show the same information as in the top panel, but averaged over four consecutive strips (Av_4). In general, the number of strips chosen for averaging is limited by the number of strips between the rise and the fall of the ΔE trace. Having been applied before for a study of the $^{23}\text{Na}(\alpha, p)^{26}\text{Mg}$ and $^{23}\text{Na}(\alpha, n)^{26}\text{Al}$ reactions [25], this technique is explained in more detail in Ref. [28].

Figure 3 represents a two-dimensional plot, where a ten-strip average (Av_{10}) has been plotted against a nine-strip average (Av_9) for events occurring in strip 5 of the detector during a 1.5 day long run. Moreover, the one-dimensional (1D) projection of Av_{10} has been highlighted in Fig. 4 where three peaks corresponding to (α, α') , (α, p) , and (α, n) reactions on ^{38}Ar can be clearly identified. The red curve shows the total fit to the spectrum and the black dashed lines show the individual Gaussian fits to the three peaks. The overlap between the peaks leads to an overall uncertainty of less than 5% in the counts under each peak. In this manner, the number of events associated with the different reaction channels were obtained for the first eight anode segments allowing determination of the $^{38}\text{Ar}(\alpha, n)^{41}\text{Ca}$ and $^{38}\text{Ar}(\alpha, p)^{41}\text{K}$ reaction cross sections.

The angle- and excitation-energy-integrated cross sections of the $^{38}\text{Ar}(\alpha, n)^{41}\text{Ca}$ and $^{38}\text{Ar}(\alpha, p)^{41}\text{K}$ reactions are displayed in Fig. 5 by the blue circles (α, n) and red circles (α, p) , respectively. The uncertainties in the cross sections are statistical and those in the center-of-mass energies are due to the energy range (~ 330 keV) covered in each strip as determined using the SRIM code [29]. The dashed and dotted lines represent the predicted cross sections calculated using the statistical model from Ref. [30] and the TALYS default code, respectively.

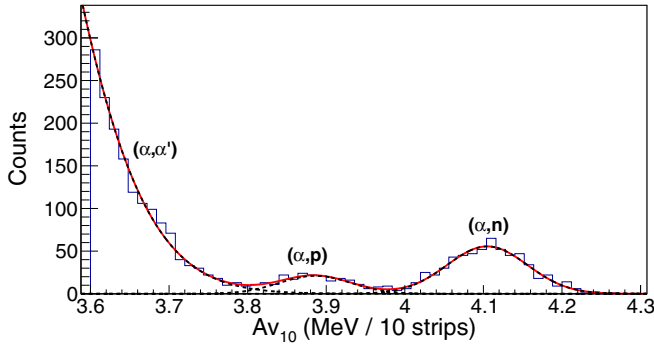


FIG. 4. One-dimensional projection of ΔE values for events occurring in strip 5 averaged over ten consecutive strips (Av_{10}) highlighting three peaks corresponding to events from (α, α') , (α, p) , and (α, n) reactions on ^{38}Ar . The red curve represents the total fit to the spectrum and the black dashed lines represent the individual Gaussian fits to each peak.

In Fig. 5, an effective energy has been calculated instead of using the energy in the middle of each strip in order to take into account the energy dependence of the cross section. The details of the comparison to statistical-model calculations, the astrophysical reaction rate, and implications are discussed below.

III. COMPARISON TO STATISTICAL-MODEL CALCULATIONS

The cross sections of α -induced reactions on ^{38}Ar have been calculated within the statistical model (StM). It is a basic prerequisite for the applicability of the StM that the level density in the compound nucleus is sufficiently high. The experimental data are average cross sections within the experimental energy range ΔE , which is defined by the energy width of the beam, the energy loss of the projectiles in the target, and the binning

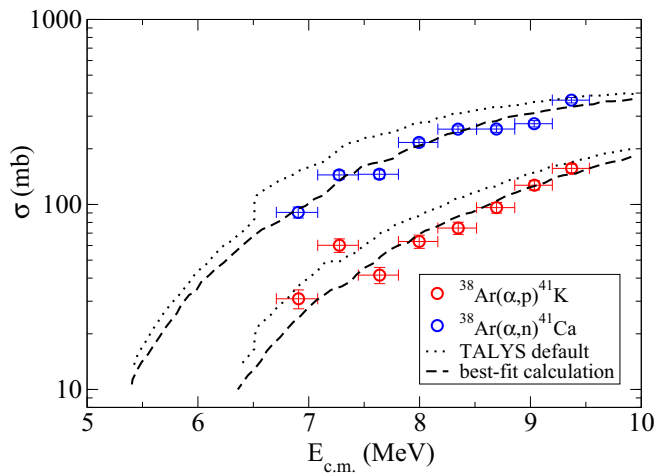


FIG. 5. Excitation functions of the $^{38}\text{Ar}(\alpha, n)^{41}\text{Ca}$ (blue circles) and $^{38}\text{Ar}(\alpha, p)^{41}\text{K}$ (red circles) reactions determined in the present study in comparison with the statistical-model calculations: TALYS default (dotted lines) and best-fit calculation (dashed lines, see Sec. III).

of the data points. If the level density is not sufficiently high, the excitation functions may be affected by individual resonances. As the experimental excitation functions show a relatively smooth energy dependence [except for the two lowest data points of the (α, p) reaction], the StM should be applicable for the present data although the level densities in the semimagic ^{38}Ar ($N = 20$) target and ^{42}Ca ($Z = 20$) compound nuclei remain relatively small.

In a schematic notation the reaction cross section in the Hauser-Feshbach (HF) StM [31] is proportional to

$$\sigma(\alpha, X)_{\text{HF}} \sim \frac{T_{\alpha,0} T_X}{\sum_i T_i} = T_{\alpha,0} \times b_X \quad (1)$$

with the transmission coefficients T_i into the i th open channel and the branching ratio $b_X = T_X / \sum_i T_i$ for the decay into the channel X . The total transmission is given by the sum over all contributing channels: $T_{\text{tot}} = \sum_i T_i$. The T_i are calculated from optical potentials for the particle channels and from the γ -ray strength function for the photon channel. The T_i include contributions of all final states j in the respective residual nucleus in the i th exit channel. $T_{\alpha,0}$ refers to the entrance channel with the target nucleus ^{38}Ar in the ground state. For details on the definition of the T_i , see Ref. [32].

Additional correlations between the incident and outgoing waves are taken into account by a so-called width fluctuation correction factor (WFCF) $W_{\alpha X}$, which typically enhances the compound-elastic cross section:

$$\sigma(\alpha, X) = \sigma(\alpha, X)_{\text{HF}} \times W_{\alpha X}. \quad (2)$$

It is obvious from Eqs. (1) and (2) that the calculated cross sections depend mainly on the α -nucleus optical-model potential (A-OMP), which defines the transmission T_α (and thus the total α -induced reaction cross section σ_{reac}) and on the nucleon optical-model potentials (N-OMP), which define the transmissions T_n and T_p (and thus the branching toward either the (α, n) or (α, p) channel). The sensitivity to the chosen level density and γ -ray strength remains very minor for the reactions in this study. A precise mathematical definition of sensitivities is given in Ref. [33]. The results from the statistical model code NON-SMOKER are available online [34] and confirm the qualitative discussion above.

In the mass range $20 \leq A \leq 50$ a more or less generic behavior of α -induced reaction cross sections is found [30] where σ_{reac} is approximately given by the sum of the (α, n) and (α, p) cross sections, and σ_{reac} is dominated with $\gtrsim 90\%$ by either the (α, n) or the (α, p) channel. Interestingly, the situation for ^{38}Ar is different from most of the other nuclei in the $20 \leq A \leq 50$ mass range. Because the Q values for the otherwise dominating (α, n) or (α, p) channels are both significantly negative ($Q_n = -5.22$ MeV and $Q_p = -4.02$ MeV), at the energies under study the ^{42}Ca compound nucleus decays also back into the entrance α channel with a noticeable probability. Consequently, the width fluctuation correction factor $W_{\alpha X}$ is more important here than for other nuclei in this mass range.

Very recently, a complete survey of the parameter space of the TALYS code was provided for α -induced reaction cross sections on ^{64}Zn [35]. The same procedure has been applied here for ^{38}Ar to find the best set of parameters out of almost

7000 combinations of A-OMPs, N-OMPs, γ -ray strength functions, and level densities. It is found that the simple four-parameter A-OMP by McFadden and Satchler [36] in combination with the TALYS default N-OMP by Koning and Delaroche [37] provides the best description of the data (see Fig. 5, dashed lines). These best-fit parameters will be used in the following calculation of astrophysical reaction rates.

A calculation with the TALYS default parameters clearly deviates from the experimental data. In particular, the (α, n) cross section is overestimated, and a kink around 6.5 MeV indicates the inaccurate treatment of the width fluctuation correction in the default calculation (dotted lines in Fig. 5).

A full discussion of the statistical-model calculations exceeds the scope of the present study and will be presented in a forthcoming paper. This will also include more details on the performance of various global α -nucleus potentials which are the most important ingredients for the $^{38}\text{Ar}(\alpha, n)^{41}\text{Ca}$ and $^{38}\text{Ar}(\alpha, p)^{41}\text{K}$ reactions.

IV. ASTROPHYSICAL REACTION RATE AND IMPLICATIONS

A. Calculation of the astrophysical reaction rate

The astrophysical reaction rates $N_A \langle \sigma v \rangle$ of the $^{41}\text{Ca}(n, \alpha)^{38}\text{Ar}$ and $^{41}\text{K}(p, \alpha)^{38}\text{Ar}$ reactions can be calculated by detailed balance [38] using the $^{38}\text{Ar}(\alpha, n)^{41}\text{Ca}$ and $^{38}\text{Ar}(\alpha, p)^{41}\text{K}$ reaction cross sections determined in the previous section. This procedure is described in detail below.

All nuclei in the vicinity of the $N = 20$ shell closure are characterized by relatively high-lying first excited states (^{38}Ar : 2^+ , 2167.6 keV; ^{41}K : $1/2^+$, 980.5 keV; ^{41}Ca : $3/2^-$, 1942.9 keV). This leads to the peculiar situation that the ground-state contributions are dominating for all reactions at astrophysically relevant energies; i.e., in the $^{38}\text{Ar}(\alpha, p)^{41}\text{K}$ and $^{38}\text{Ar}(\alpha, n)^{41}\text{Ca}$ reactions the (α, p_0) and (α, n_0) channels are dominating, leading to the $^{41}\text{K}(3/2^+)$ and $^{41}\text{Ca}(7/2^-)$ ground states, and the $^{41}\text{K}(p, \alpha)^{38}\text{Ar}$ and $^{41}\text{Ca}(n, \alpha)^{38}\text{Ar}$ reactions preferentially populate the $^{38}\text{Ar} 0^+$ ground state. As the dominating (α, p_0) and (p, α_0) cross sections are directly related by time reversal, there is also an approximate relation between the total (α, p) and (p, α) cross sections. The same holds for the (α, n) and (n, α) reactions.

In addition, the astrophysical reaction rates $N_A \langle \sigma v \rangle$ of forward and reverse reactions are related by detailed balance. In combination with the findings of the previous paragraph, this allows sensitive tests of the numerical rate calculations.

In a first step, for both reactions, $^{38}\text{Ar}(\alpha, p)^{41}\text{K}$ and $^{38}\text{Ar}(\alpha, n)^{41}\text{Ca}$, excitation functions were calculated in 1-keV steps from threshold to 18 MeV using the best-fit parameters of the previous section. The reaction rates $N_A \langle \sigma v \rangle$ are then calculated by numerical integration of these excitation functions. This leads to stable results for $T_9 \gg 0.1$. However, below $T_9 \approx 0.1$ the rates of the (α, p) and (α, n) reactions drop below $10^{-200} \text{ cm}^3 \text{ s}^{-1} \text{ mole}^{-1}$ and become extremely sensitive to the cross sections in the first few keV above the respective (α, p) and (α, n) thresholds.

Therefore, the cross sections of the reverse $^{41}\text{K}(p, \alpha)^{38}\text{Ar}$ and $^{41}\text{Ca}(n, \alpha)^{38}\text{Ar}$ reactions were calculated from 1 keV–

TABLE I. Astrophysical reaction rate $N_A \langle \sigma v \rangle$ of the $^{41}\text{K}(p, \alpha)^{38}\text{Ar}$ and $^{41}\text{Ca}(n, \alpha)^{38}\text{Ar}$ reactions. All rates are given in units of $\text{cm}^3 \text{ s}^{-1} \text{ mole}^{-1}$.

T_9	$^{41}\text{K}(p, \alpha)^{38}\text{Ar}$	$^{41}\text{Ca}(n, \alpha)^{38}\text{Ar}$
0.1	2.08×10^{-13}	$3.69 \times 10^{+7}$
0.2	8.57×10^{-8}	$3.21 \times 10^{+7}$
0.5	3.56×10^{-2}	$2.83 \times 10^{+7}$
1.0	$4.96 \times 10^{+1}$	$2.76 \times 10^{+7}$
2.0	$8.68 \times 10^{+3}$	$3.03 \times 10^{+7}$
5.0	$8.89 \times 10^{+5}$	$5.15 \times 10^{+7}$
10.0	$9.11 \times 10^{+6}$	$1.44 \times 10^{+8}$

10 MeV in 1 keV steps. Exactly the same parameters were used which were determined as best-fit parameters for the new (α, p) and (α, n) data, as described in Sec. III. At very low energies, charged-particle-induced cross sections become very tiny because of the Coulomb barrier, and in practice it is impossible to measure these tiny cross sections. In addition, calculations of these tiny cross sections become numerically delicate. Thus, for the lowest energies below 100 keV, the (p, α) cross sections were obtained as follows. The calculated cross sections between 100 and 500 keV were converted to the astrophysical S factor, which turns out to be a smooth function of energy. The calculated S factor was then extended down to lowest energies using a second-order polynomial, leading to a S factor at zero energy of $S(0) = 1.83 \times 10^7 \text{ keV b}$. From the excitation functions of the (p, α) and (n, α) cross sections the rates $N_A \langle \sigma v \rangle$ of the (p, α) and (n, α) reactions were calculated by numerical integration. In addition, the stellar enhancement factor (SEF) was taken from the calculations by Rauscher and Thielemann [38]. The SEF remains very close to unity up to $T_9 \approx 3\text{--}4$ for both reactions and does not deviate by more than about 30% from unity up to $T_9 = 10$. These recommended results are given in Table I, and some comparisons to the new recommended rates are shown in Fig. 6. Analytical fits have been made to the recommended rates using the standard parametrization as used, e.g., in Eq. (16) of Ref. [38] or in the REACLIB database [39]. The resulting a_i parameters and information on the valid temperature range are listed in Table II.

As a final check of the numerical analysis, the rates for the (p, α) reaction and for the (α, p) reaction (both calculated by numerical integration of the respective cross sections) were compared. It was found that the rates follow the expected ratio using detailed balance. The same result was found for the (n, α) and (α, n) rates. This confirms that all results are numerically stable in the given temperature range within a few percent.

Up to now, the rates of the $^{41}\text{K}(p, \alpha)^{38}\text{Ar}$ and $^{41}\text{Ca}(n, \alpha)^{38}\text{Ar}$ reactions were (e.g., in REACLIB) adopted from Sevier *et al.* [24]. In their experiment the cross section of the $^{41}\text{K}(p, \alpha_0)^{38}\text{Ar}$ reaction was determined at low center-of-mass energies from 0.8–2.6 MeV. However, the excitation function was determined only at one particular angle, probably assuming isotropy (nothing is stated on corrections for the expected angular distributions). In addition, the experiment suffered from a high background from elastically scattered protons from their KBr target and from the gold backing. The resulting cross sections

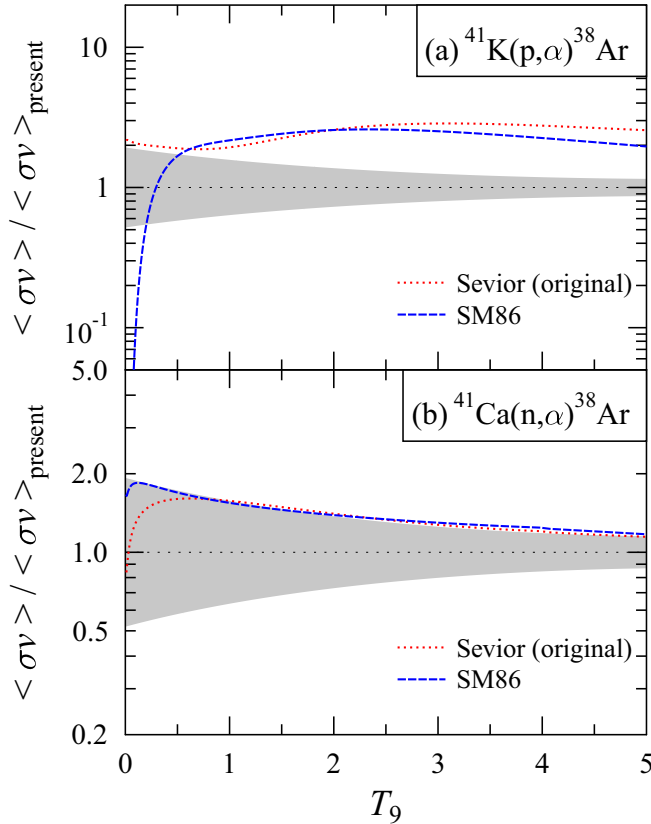


FIG. 6. Comparison of reaction rates $N_A\langle\sigma v\rangle$ for the (a) $^{41}\text{K}(p,\alpha)^{38}\text{Ar}$ and (b) $^{41}\text{Ca}(n,\alpha)^{38}\text{Ar}$ reactions. The rates of Sevior *et al.* [24] from their original fit and from a later fit in REACLIB (usually referred to as “SM86”) are normalized to the new recommended rate. The gray-shaded uncertainties are discussed at the end of Sec. IV A. Note the different scale factors in the top and the bottom panels. See text for further discussion.

show a significant scatter of at least a factor of two to three (see Fig. 3 of Ref. [24]).

It was found in Ref. [24] that the statistical model parameters had to be adjusted to achieve calculated cross sections in the center of the experimental data, whereas the default calculation is at the lower end of the experimental data. For the $^{41}\text{Ca}(n,\alpha)^{38}\text{Ar}$ cross sections, which were not measured in Ref. [24], a calculation using the same modified statistical model parameters deduced from the $^{41}\text{K}(p,\alpha)^{38}\text{Ar}$ cross sections was performed. From these cross sections, astrophysical reaction rates $N_A\langle\sigma v\rangle$ were calculated and presented in Tables 3 and 4 of Ref. [24] for temperatures from $T_9 = 0.5$ –10, and analytical fits were provided using the parametrization of

Ref. [40]. Later, the given rates for $0.5 \leq T_9 \leq 10$ were refitted using the nowadays adopted parameterization [38,39].

The results from our experiment for the $^{41}\text{K}(p,\alpha)^{38}\text{Ar}$ cross sections agree roughly with the earlier statistical model calculation in Ref. [24] using the default parameters; thus, the resulting reaction rate is significantly lower than the recommendation in Ref. [24] (see Fig. 6). Furthermore it is found that the REACLIB fit to the Sevior *et al.* data dramatically deviates from Sevior’s original fit for temperatures below $T_9 = 0.5$ because the REACLIB fit was not constrained from the data in Table 3 of Ref. [24]; obviously, the REACLIB fit should not be used at temperatures below $T_9 \approx 0.5$.

For the $^{41}\text{Ca}(n,\alpha)^{38}\text{Ar}$ reaction, similar results as for the $^{41}\text{K}(p,\alpha)^{38}\text{Ar}$ reaction are found, although the deviations are smaller for the (n,α) reaction than for the (p,α) reaction. For the (n,α) reaction the present result is about 30% lower than Sevior’s recommendation. Contrary to Sevior’s recommendation, the present (n,α) rate calculation is now based on experimental data for the (α,n) reaction, which essentially defines the rate for the (n,α) reaction.

At the upper end of the temperature range under study ($T_9 \sim 10$) the uncertainties of the present astrophysical reaction rate can be estimated directly from the uncertainties of our experimental (α,p) and (α,n) data, which is of the order of 10–20%. At lower temperatures $N_A\langle\sigma v\rangle$ is based on the energy dependence of our new calculation, which is confirmed by the experimental energy dependence of the (p,α) data of Ref. [24] down to about $T_9 \approx 1$. Thus, the uncertainty should not exceed 30%. A careful estimate of the uncertainty down to $T_9 = 1$ gives a factor of 0.7 as a lower limit and a factor of two as an upper limit (where the latter takes into account that the experimental (p,α) data of Ref. [24] are on average within their large scatter above the new calculation). Below $T_9 \approx 1$, the recommended rate is solely based on the energy dependence of the calculated cross sections, and here a factor of two should be a reasonable estimate for the uncertainty. The uncertainties of the rates from the present study are shown as gray-shaded areas in Fig. 6.

The uncertainties of the $^{41}\text{K}(p,\alpha)^{38}\text{Ar}$ and $^{41}\text{Ca}(n,\alpha)^{38}\text{Ar}$ reaction rates from Ref. [24] are significant based on the large scatter of their $^{41}\text{K}(p,\alpha)^{38}\text{Ar}$ reaction cross section data. However, they are not adequately defined in Ref. [24], which makes it difficult to get a concrete estimate of their reaction rate uncertainties and, hence, can not be plotted in Fig. 6 for comparison.

B. Astrophysical implications

We now discuss the implications of the new reaction rate by considering its effect on explosive nucleosynthesis in core-collapse supernovae. Using an explosion energy of 1.0

TABLE II. Fit parameters a_i for the reaction rate $N_A\langle\sigma v\rangle$.

Reaction	T_9 range	Accuracy	a_0	a_1	a_2	a_3	a_4	a_5	a_6
$^{41}\text{K}(p,\alpha)^{38}\text{Ar}$	0.01–10.0	$\lesssim 10\%$	39.6775	−0.0232394	−26.9012	−8.90413	−0.0554046	0.0441426	2.85219
$^{41}\text{K}(p,\alpha)^{38}\text{Ar}$	0.1–10.0	$\lesssim 5\%$	64.4107	−0.681143	9.28681	−73.161	4.26053	−0.235892	31.8226
$^{41}\text{Ca}(n,\alpha)^{38}\text{Ar}$	0.01–10.0	$\lesssim 3\%$	17.6614	−0.0072314	0.673546	−1.56523	0.38023	−0.0115058	0.403521

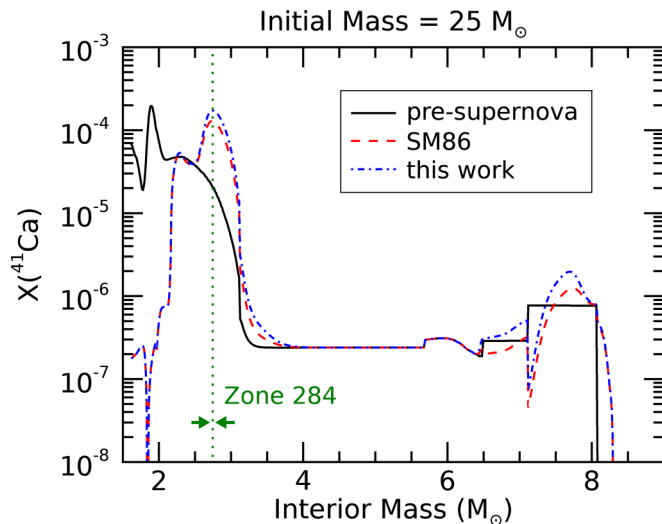


FIG. 7. Final ^{41}Ca mass fraction as a function of interior mass coordinate one year after the 1.0 B explosion of presupernova model s28a28 from Ref. [41] for the indicated reaction networks.

B (i.e., 10^{51} erg), and other parameters as chosen in Ref. [23], we applied our simple type II supernova code to a $25\text{-}M_{\odot}$ presupernova (evolved until onset of core collapse) star model [23,41]. From the thermodynamic trajectories derived from our explosion model, we computed the resulting nucleosynthesis over all 764 zones available in the presupernova star.

Figure 7 shows the mass fraction of ^{41}Ca as a function of the interior mass coordinate within the ejecta of the star using the default REACLIB V2.0 (“SM86”) reaction-rate data snapshot [39] (which includes rates from Ref. [24] for the $^{41}\text{Ca}(n,\alpha)^{38}\text{Ar}$ and $^{41}\text{K}(p,\alpha)^{38}\text{Ar}$ reactions) and the same snapshot updated with our new rates. By default, we follow the nucleosynthesis for one year after the explosion to allow all short-lived radioactive nuclides (with lifetime less than roughly one month) to decay fully to their daughters. This is not important for ^{41}Ca , which has a very small contribution from radioactive progenitors, but it can be for other species. The new reaction rates increase the yield of ^{41}Ca by up to $\sim 20\%$ in several zones where a plethora of neutrons are generated during the explosion, the peak yield occurring near $2.75 M_{\odot}$. The total ejected mass of ^{41}Ca with our new rates is $7.50 \times 10^{-5} M_{\odot}$, while $6.20 \times 10^{-5} M_{\odot}$ of ^{41}Ca is ejected when using the default REACLIB V2.0 rates; thus, our new rates lead to an increase of $\sim 20\%$ in the ^{41}Ca mass fraction.

Figure 8 shows the mass fraction of ^{41}Ca as a function of time in zone 284 at an interior mass coordinate of $M_r = 2.7439 M_{\odot}$. The contrasting curves show the time dependence using the default REACLIB V2.0 reaction-rate data snapshot and the same snapshot updated with our new rates for the $^{41}\text{Ca}(n,\alpha)^{38}\text{Ar}$ and $^{41}\text{K}(p,\alpha)^{38}\text{Ar}$ reactions together and individually. In all cases, the ^{41}Ca mass fraction rises abruptly from its presupernova value in the zone at a time of $t = 0.72$ s after the supernova shock wave is launched, the temperature peaking near $T_9 = 2.73$. The ^{41}Ca mass fraction then declines slightly before freezing out at $t \sim 1$ s as the shocked matter expands and cools. Because the temperature at this time is

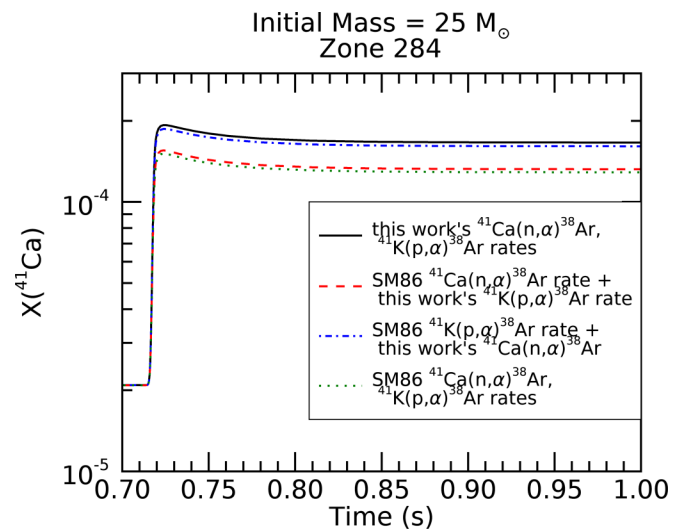


FIG. 8. Time evolution of the ^{41}Ca mass fraction in zone 284 during the 1.0 B explosion of presupernova model s25a28 from Ref. [41] for the indicated reaction networks.

$T_9 \sim 2.28$ and much greater than $T_9 = 0.1$, the aforementioned difficulties in computing the rates for $T_9 < 0.1$ do not affect the resulting ^{41}Ca abundance. With our new rates, the ^{41}Ca mass fraction achieves a $\sim 20\%$ increase over that produced from the REACLIB V2.0 default rates. Though the new $^{41}\text{K}(p,\alpha)^{38}\text{Ar}$ rate by itself contributes to an increase in ^{41}Ca , the bulk of the change is attributable to the updated $^{41}\text{Ca}(n,\alpha)^{38}\text{Ar}$ rate.

Figure 9 is an integrated currents diagram for zone 284 after utilizing our new rates in the REACLIB V2.0 snapshot. The integrated current is the net number of nuclei per nucleon that undergo the indicated reaction during the calculation (e.g., Ref. [23]). The arrow thickness is proportional to the integrated current. From the figure we can deduce that the bulk of ^{41}Ca production comes from neutron capture by ^{40}Ca . Destruction of ^{41}Ca occurs predominantly via the $^{41}\text{Ca}(n,\alpha)^{38}\text{Ar}$ channel. Since the arrows leading into ^{41}Ca sum to a greater thickness than the arrows leading out, the ^{41}Ca abundance (and, likewise, its mass fraction) accordingly sustains a positive net change, visible in Fig. 8.

Figure 10 is an integrated-currents difference diagram for zone 284. In particular, this figure shows the integrated currents for the calculation with our new rates minus the integrated currents for the calculation with the default REACLIB V2.0 rates. If the difference is negative, the arrow changes direction (e.g., Ref. [23]). The biggest difference in the calculations is the strong arrow from ^{38}Ar to ^{41}Ca . As the actual integrated current proceeds from ^{41}Ca to ^{38}Ar (see Fig. 9), there must be less current from the $^{41}\text{Ca}(n,\alpha)^{38}\text{Ar}$ reaction in the calculation with our new rates. Our lower rate for the (n,α) reaction inhibits destruction of ^{41}Ca by neutron captures and, in turn, generates a smaller current.

As less ^{41}Ca nuclei are destroyed by the (n,α) reaction with our new rates, more are available to flow into the creation of ^{42}Ca via the $^{41}\text{Ca}(n,\gamma)^{42}\text{Ca}$ channel. The arrow from ^{41}Ca to ^{42}Ca in Fig. 10 accounts for this enhanced current relative to the calculation with the default REACLIB V2.0 rates. In

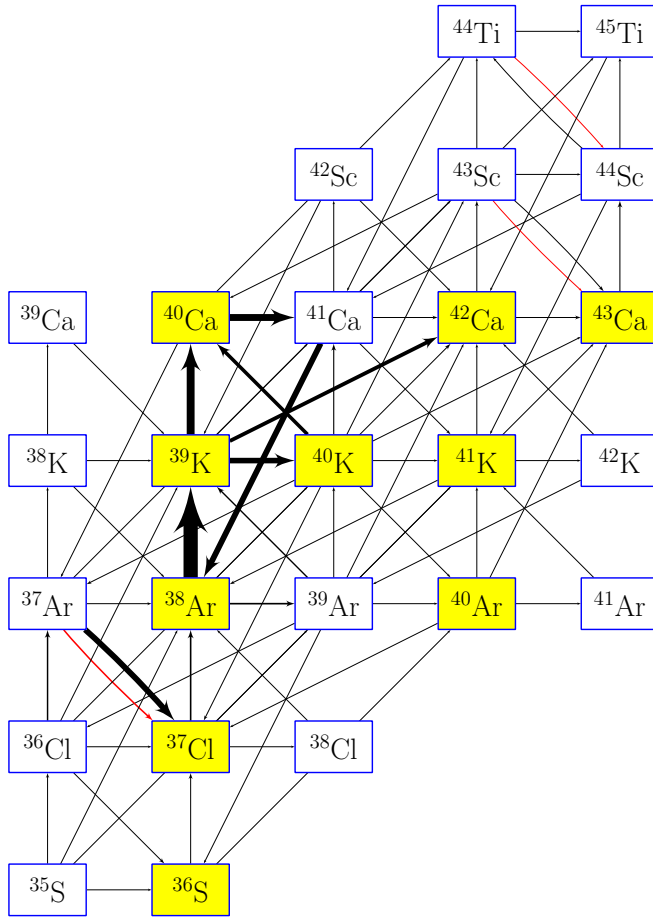


FIG. 9. Integrated currents for zone 284 after the 1.0 B explosion of pre-supernova model s25a28 from Ref. [41] for the REACLIB V2.0 reaction network updated with the rates of this work.

the same vein, the larger number of ^{41}Ca nuclei causes a higher reverse $^{41}\text{Ca}(\gamma, n)^{40}\text{Ca}$ flow, which leads to a reduced net $^{40}\text{Ca}(n, \gamma)^{41}\text{Ca}$ flow. The diminished net flow to ^{41}Ca is illustrated by the arrow from ^{41}Ca to ^{40}Ca in Fig. 10.

Figure 10 also shows an arrow from ^{38}Ar to ^{41}K . During each calculation, ^{41}K is destroyed in the flow to ^{38}Ar . Our lower rate for $^{41}\text{K}(p, \alpha)^{38}\text{Ar}$, however, slows such destruction, allowing the ^{41}K mass fraction to remain at a higher level in the corresponding calculation. The $^{41}\text{K}(p, n)^{41}\text{Ca}$ flow, then, is better able to counter the reverse $^{41}\text{Ca}(n, p)^{41}\text{K}$ flow that destroys ^{41}Ca . A reduction in the net (n, p) flow follows, with the arrow from ^{41}K to ^{41}Ca in Fig. 10 signifying this difference between the two calculations. This by itself accounts for the slightly larger mass fraction of ^{41}Ca in the calculation with only the rate for the $^{41}\text{K}(p, \alpha)^{38}\text{Ar}$ reaction updated (see Fig. 8).

As discussed in Ref. [23], the sum of thicknesses of arrows into a species minus the sum of thicknesses of arrows out of a species in an integrated-current difference diagram is proportional to the difference in final abundance of that species between the two calculations. Since the arrows leading into ^{41}Ca sum to a greater thickness than the arrows leading out in Fig. 10, the final abundance (and, likewise, the mass fraction) of ^{41}Ca is greater in the calculation with our new rates, as

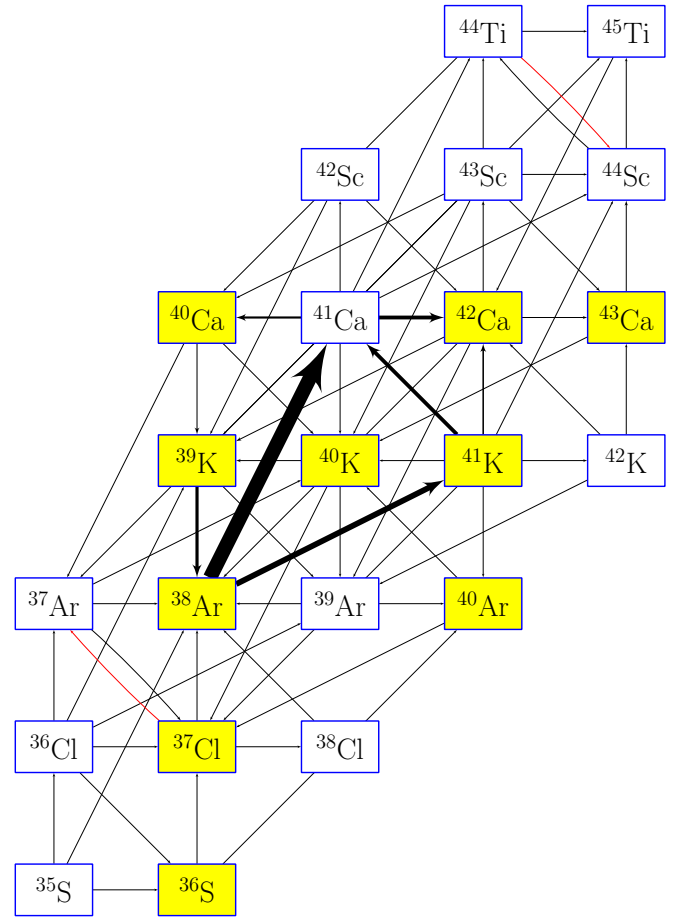


FIG. 10. Integrated current differences between the REACLIB V2.0 reaction network and REACLIB V2.0 reaction network updated with the rates of this work for zone 284 after the 1.0 B explosion of pre-supernova model s25a28 from Ref. [41]. As discussed in the text, the strength of an arrow in this figure represents how much greater the integrated current is in the calculation with the updated reaction rates than in the calculation with the default reaction rate set (REACLIB V2.0 only). A reversed arrow relative to the integrated current graph (Fig. 9) indicates the integrated current from the default reaction rate set is greater than in the calculation with the default set updated with our new reaction rates.

evident in Fig. 8. Although an increase in the destructive flows via (n, γ) , (γ, n) , and (n, p) reactions on ^{41}Ca also arises in the wake of these reduced rates, their contribution to destroying ^{41}Ca nuclei cannot offset the amount of ^{41}Ca nuclei left behind upon lowering the $^{41}\text{Ca}(n, \alpha)^{38}\text{Ar}$ rate.

A similar analysis holds for zones between $M_r = 6.5\text{--}7.0 M_\odot$ and between $M_r = 7.5\text{--}8.0 M_\odot$, although in these regions the role of the $^{41}\text{K}(p, \alpha)^{38}\text{Ar}$ reaction is limited due to the drop off in the postshock temperatures and the lower abundance of free protons; resulting in a lower destruction of ^{41}Ca by the reduced (n, α) rate, which produces a higher final ^{41}Ca abundance. In all cases in these outer zones, freeze out occurred at $T_9 > \sim 0.4$, so uncertainties in the investigated reaction rates below $T_9 = 0.1$ do not affect our calculated abundances.

Of course, this analysis incorporated a single, yet representative, model of supernova production for ^{41}Ca . A reduced (n, α) rate may also catalyze a growth of the ^{41}Ca abundance in the presupernova star, which is not addressed in our calculations. However, much of the integrated ^{41}Ca yield from a massive star occurs via explosive nucleosynthesis (in the interior mass range of $M_r = 2.5\text{--}3.0 M_\odot$ for the model presented above) and massive stars are the dominant contributors of ^{41}Ca to the interstellar medium, prompting us to suggest our new reaction rates will lead to a $\sim 20\%$ increase in the yield of ^{41}Ca from galactic stars.

V. CONCLUSIONS

The time-inverse $^{38}\text{Ar}(\alpha, n)^{41}\text{Ca}$ and $^{38}\text{Ar}(\alpha, p)^{41}\text{K}$ cross sections were measured simultaneously in inverse kinematics using a multisampling ionization chamber with $\sim 100\%$ detection efficiency for the reaction products. Both cross sections were found to be in good agreement with the statistical model calculation from Ref. [30]. Contrary to Sevier *et al.* [24], the new $^{41}\text{Ca}(n, \alpha)^{38}\text{Ar}$ and $^{41}\text{K}(p, \alpha)^{38}\text{Ar}$ reaction rates are

based on experimental data with well-defined experimental uncertainties. These new rates suggest a $\sim 20\%$ increase in the yield of ^{41}Ca from massive stars via explosive nucleosynthesis and perhaps a similar increase in the presupernova nucleosynthesis yield that gets ejected with little modification during the explosion. This increase in the modeled production of ^{41}Ca in massive stars supports a stellar origin for the inferred ^{41}Ca abundance in the early solar system and affects constraints on the mixing of supernova zones from abundances in low-density presolar graphite grains.

ACKNOWLEDGMENTS

This work was supported by the U.S. Department of Energy, Office of Science, Office of Nuclear Physics, under Contract No. DE-AC02-06CH11357, by NASA Grant No. NNX14AI25G, and by OTKA (K108459 and K120666). D.S.G. acknowledges the support by the U.S. Department of Energy, Office of Nuclear Physics, under Grant No. DE-FG02-96ER40978. This research used resources of ANL's ATLAS facility, which is a DOE Office of Science User Facility.

-
- [1] K. McKeegan and A. Davis, in *Treatise on Geochemistry*, edited by H. D. Holland and K. K. Turekian (Pergamon, Oxford, 2007), pp. 1–38.
- [2] M.-C. Liu, *Geochim. Cosmochim. Acta* **201**, 123 (2017).
- [3] G. R. Huss, B. S. Meyer, G. Srinivasan, J. N. Goswami, and S. Sahijpal, *Geochim. Cosmochim. Acta* **73**, 4922 (2009).
- [4] G. Wasserburg, M. Busso, R. Gallino, and K. Nollett, *Nucl. Phys. A* **777**, 5 (2006).
- [5] M. Gounelle, F. H. Shu, H. Shang, A. E. Glassgold, K. E. Rehm, and T. Lee, *Astrophys. J.* **640**, 1163 (2006).
- [6] G. Srinivasan, S. Sahijpal, A. Ulyanov, and J. Goswami, *Geochim. Cosmochim. Acta* **60**, 1823 (1996).
- [7] S. Sahijpal and J. N. Goswami, *Astrophys. J. Lett.* **509**, L137 (1998).
- [8] S. Sahijpal, J. Goswami, and A. Davis, *Geochim. Cosmochim. Acta* **64**, 1989 (2000).
- [9] A. P. Boss, *Astrophys. J.* **660**, 1707 (2007).
- [10] A. P. Boss, *Astrophys. J.* **739**, 61 (2011).
- [11] M.-C. Liu, M. Chaussidon, G. Srinivasan, and K. D. McKeegan, *Astrophys. J.* **761**, 137 (2012).
- [12] E. D. Young, J. I. Simon, A. Galy, S. S. Russell, E. Tonui, and O. Lovera, *Science* **308**, 223 (2005).
- [13] G. Srinivasan and M. Chaussidon, *Earth Planet. Sci. Lett.* **374**, 11 (2013).
- [14] M. Ito, H. Nagasawa, and H. Yurimoto, *Meteorit. Planet. Sci.* **41**, 1871 (2006).
- [15] G. J. Wasserburg, J. Wimpenny, and Q.-Z. Yin, *Meteorit. Planet. Sci.* **47**, 1980 (2012).
- [16] D. Wielandt, K. Nagashima, A. N. Krot, G. R. Huss, M. A. Ivanova, and M. Bizzarro, *Astrophys. J. Lett.* **748**, L25 (2012).
- [17] M. Gounelle, M. Chaussidon, and C. Rollion-Bard, *Astrophys. J. Lett.* **763**, L33 (2013).
- [18] J. H. Kastner and P. C. Myers, *Astrophys. J.* **421**, 605 (1994).
- [19] D. D. Clayton and L. R. Nittler, *Annu. Rev. Astron. Astrophys.* **42**, 39 (2004).
- [20] P. Hoppe, R. Strebler, P. Eberhardt, S. Amari, and R. S. Lewis, *Science* **272**, 1314 (1996).
- [21] L. R. Nittler, S. Amari, E. Zinner, S. E. Woosley, and R. S. Lewis, *Astrophys. J. Lett.* **462**, L31 (1996).
- [22] S. Amari, E. Zinner, and R. S. Lewis, *Astrophys. J. Lett.* **470**, L101 (1996).
- [23] M. J. Bojazi and B. S. Meyer, *Phys. Rev. C* **89**, 025807 (2014).
- [24] M. Sevier, L. Mitchell, C. Tingwell, and D. Sargood, *Nucl. Phys. A* **454**, 128 (1986).
- [25] M. L. Avila, K. E. Rehm, S. Almaraz-Calderon, A. D. Ayangeakaa, C. Dickerson, C. R. Hoffman, C. L. Jiang, B. P. Kay, J. Lai, O. Nusair *et al.*, *Phys. Rev. C* **94**, 065804 (2016).
- [26] P. F. F. Carnelli, S. Almaraz-Calderon, K. E. Rehm, M. Albers, M. Alcorta, P. F. Bertone, B. Digiiovine, H. Esbensen, J. O. F. Niello, D. Henderson *et al.*, *Phys. Rev. Lett.* **112**, 192701 (2014).
- [27] P. Carnelli, S. Almaraz-Calderon, K. Rehm, M. Albers, M. Alcorta, P. Bertone, B. Digiiovine, H. Esbensen, J. F. Niello, D. Henderson *et al.*, *Nucl. Instrum. Methods Phys. Res., Sect. A* **799**, 197 (2015).
- [28] M. L. Avila, K. E. Rehm, S. Almaraz-Calderon, A. D. Ayangeakaa, C. Dickerson, C. R. Hoffman, C. L. Jiang, B. P. Kay, J. Lai, O. Nusair *et al.*, *Nucl. Instrum. Methods Phys. Res., Sect. A* **859**, 63 (2017).
- [29] J. F. Ziegler, M. Ziegler, and J. Biersack, *Nucl. Instrum. Methods Phys. Res., Sect. B* **268**, 1818 (2010).
- [30] P. Mohr, *Eur. Phys. J. A* **51**, 56 (2015).
- [31] W. Hauser and H. Feshbach, *Phys. Rev.* **87**, 366 (1952).
- [32] T. Rauscher, *Int. J. Mod. Phys. E* **20**, 1071 (2011).
- [33] T. Rauscher, *Astrophys. J. Suppl. Ser.* **201**, 26 (2012).
- [34] T. Rauscher, <http://nucastro.org/webmoker.html>, computer code NONSMOKER.
- [35] P. Mohr, G. Gyürky, and Z. Fülöp, *Phys. Rev. C* **95**, 015807 (2017).
- [36] L. McFadden and G. Satchler, *Nucl. Phys.* **84**, 177 (1966).
- [37] A. Koning and J. Delaroche, *Nucl. Phys. A* **713**, 231 (2003).

- [38] T. Rauscher and F.-K. Thielemann, *At. Data Nucl. Data Tables* **75**, 1 (2000).
- [39] R. H. Cyburt, A. M. Amthor, R. Ferguson, Z. Meisel, K. Smith, S. Warren, A. Heger, R. D. Hoffman, T. Rauscher, A. Sakharuk *et al.*, *Astrophys. J. Suppl.* **189**, 240 (2010).
- [40] S. Woosley, W. A. Fowler, J. Holmes, and B. Zimmerman, *At. Data Nucl. Data Tables* **22**, 371 (1978).
- [41] T. Rauscher, A. Heger, R. D. Hoffman, and S. E. Woosley, *Astrophys. J.* **576**, 323 (2002).